Terahertz Magneto-Photocurrents in the Topological Insulator Bi_2Se_3 Probe Its Topological Surface States

Chihun In,[1,2,*] Genaro Bierhance,[1,2] Deepti Jain,[3] Tom S. Seifert,[1] Oliver Gueckstock,[1] Roberto Mantovan,[4] Seongshik Oh,[3,5] and Tobias Kampfrath[1,2]

[1] *Department of Physics and Center for Chiral Electronics (CCE), Freie Universität Berlin, 14195 Berlin, Germany*
[2] *Department of Physical Chemistry, Fritz Haber Institute of the Max Planck Society, 14195 Berlin, Germany*
[3] *Department of Physics and Astronomy, Rutgers, The State University of New Jersey, Piscataway, New Jersey 08854, USA*
[4] *CNR-IMM, Unit of Agrate Brianza, Agrate Brianza 20864, Italy*
[5] *Center for Quantum Materials Synthesis, Rutgers, The State University of New Jersey, Piscataway, New Jersey 08854, USA*

(Received 2 April 2024; revised 21 July 2026; accepted 24 July 2026; published 2 September 2026)

We study ultrafast magneto-photocurrents in a three-dimensional topological insulator. For this purpose, we excite $(In_rBi_{1-r})_2Se_3$ thin films with a femtosecond laser pulse in the presence of an external magnetic field $\boldsymbol{B}_{\text{ext}}$ up to 0.3 T parallel to the film plane. The resulting in-plane photocurrent is measured by detecting the emitted terahertz electromagnetic pulse. It is proportional and perpendicular to $\boldsymbol{B}_{\text{ext}}$. Strikingly, for $r \geq 4\%$, we observe an abrupt photocurrent reduction, which is strongly correlated with the indium-induced quenching of the topological surface states. The rise time, decay time, and amplitude of the terahertz magneto-photocurrent can consistently be explained by the following scenario: optically excited spin-polarized electrons propagate toward the film surface where the accumulated spin is converted into an in-plane charge current due to spin-velocity locking. Our results are highly relevant for contact-free probing of spin-charge conversion in systems without spontaneous magnetic order and without having to add invasive spin-source layers.

DOI: 10.1103/yvbq-rdkz

Motivation—Three-dimensional topological insulators (TIs), such as Bi_2Se_3, Bi_2Te_3, and Sb_2Te_3, are fascinating materials for both fundamental and applied reasons [1–5]. While the bulk of an ideal TI is insulating, the surface hosts topologically protected electronic surface states (TSS) with high conductivity and spin-velocity locking. As TSS enable efficient spin-to-charge-current conversion (SCC) [6–11], TIs are highly interesting for generating spin torque [12–15] and terahertz (THz) photocurrents [16–19].

However, in most of these studies [8,14–16], the TI was in contact with a ferromagnetic spin source whose impact on the TSS is elusive [20] but potentially highly invasive [21]. Therefore, methodologies to probe SCC by TSS without additional perturbing layers are very desirable.

In this Letter, we use femtosecond laser pulses to drive ultrafast photocurrents in thin films of the model TI Bi_2Se_3 under the influence of an external static in-plane magnetic field $\boldsymbol{B}_{\text{ext}}$ [Fig. 1(a)]. By detecting the resulting THz emission, we find an in-plane photocurrent proportional and perpendicular to $\boldsymbol{B}_{\text{ext}}$. Strikingly, as TSS are quenched by indium substitution of bismuth, the amplitude of the magneto-photocurrent drops by more than 95%.

We can consistently explain our observations by a scenario in which the laser pulse launches an out-of-plane bulk electron current with a spin polarization of ~0.3% owing to Pauli-type paramagnetism [22,23]. Once the spin current arrives at the surface, it is converted into a sizeable in-plane charge current because of the large SCC in the Bi_2Se_3 TSS [16–19]. Our results are highly interesting for contact-free probing of SCC in paramagnetic materials without having to add perturbing spin-source layers.

Experiment—Our Bi_2Se_3 films (thickness $d = 10$–50 QL with $1\,\text{QL} = 1$ quintuple layer ≈ 1 nm) are grown by molecular-beam epitaxy on sapphire substrates (thickness 0.5 mm) and capped by a selenium protection layer (20 nm). We further study $(In_rBi_{1-r})_2Se_3(30\text{ QL})$ films whose TSS disappear for an indium fraction of $r > 7\%$ [24–26].

Identically grown samples were characterized extensively in previous works [24–28]. Angle-resolved photoemission spectroscopy (ARPES) [24] and dc transport [27] revealed that the Fermi energy ϵ_F is located 15 meV above the bulk conduction-band bottom and 0.4 eV above the TSS Dirac point. Our THz Hall measurements (Supplemental Material Sec. I [29]) are consistent with previous dc results [25,27] and show an impact of r on the conduction-electron density.

*Contact author: chihun.in@fu-berlin.de

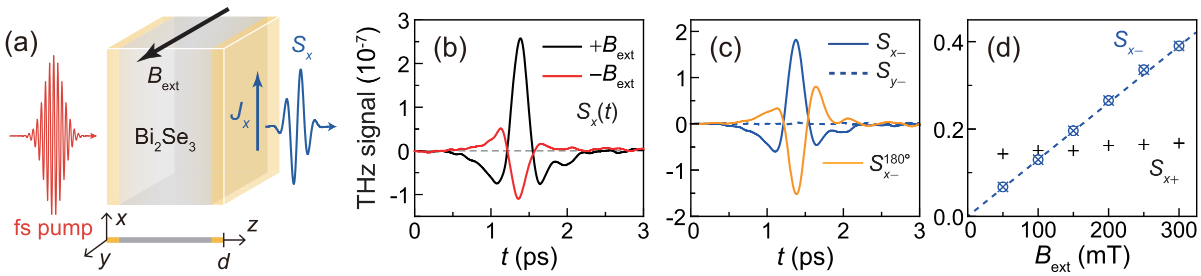

FIG. 1. (a) Schematic of the experiment. A femtosecond (fs) laser pulse drives an ultrafast photocurrent with density $\boldsymbol{j}(z,t)$ in a thin film of the TI Bi_2Se_3(16 QL) on a sapphire substrate in an external magnetic field $\boldsymbol{B}_{\rm ext} = B_{\rm ext}\boldsymbol{u}_y$. By detecting the THz electric field emitted by $\boldsymbol{j}$, we retrieve the current sheet density $\boldsymbol{J}(t) = \int \mathrm{d}z\,\boldsymbol{j}(z,t)$ vs time t. Gray and yellow regions indicate the Bi_2Se_3 bulk and TSS, respectively. (b) Typical signals $S_x(t, \pm B_{\rm ext})$ of the x-polarized THz electric-field component [see panel (a)]. (c) Signal components $S_{x-}(t)$ and $S_{y-}(t)$ odd in $B_{\rm ext}$ [Eq. (1)]. The signal $S_{x-}^{180°}(t)$ from the 180°-turned sample was corrected for the THz transmission through the substrate. (d) Root-mean-square of S_{x-} and S_{x+} vs $B_{\rm ext}$ along with a linear fit to S_{x-}.

In our setup, an external magnetic field $\boldsymbol{B}_{\rm ext} = B_{\rm ext}\boldsymbol{u}_y$ with $|B_{\rm ext}| \leq 0.3$ T is applied along the y-axis unit vector $\boldsymbol{u}_y$ [Fig. 1(a)]. Femtosecond laser pulses are normally incident onto the sample's substrate side and launch a photocurrent with density $\boldsymbol{j}(z,t)$ in the TI. The current gives rise to the emission of an electromagnetic pulse with frequencies extending into the THz range (Supplemental Material Sec. II [29]). The THz electric field is characterized by electro-optic sampling in a 1-mm-thick ZnTe (110) window [38]. Its component along $\boldsymbol{u}_x$ and $\boldsymbol{u}_y$, respectively, results in an electro-optic signal $S_x(t, B_{\rm ext})$ and $S_y(t, B_{\rm ext})$. All measurements (Figs. 1–3, 5, and 6, and Supplemental Material Secs. III–V [29]) are conducted under ambient conditions in dry air.

Photocurrent contributions—The THz signals S_x and S_y can be used to retrieve the components $J_x(t) = \boldsymbol{J}(t)\cdot\boldsymbol{u}_x$ and $J_y(t) = \boldsymbol{J}(t)\cdot\boldsymbol{u}_y$ of the photocurrent sheet density $\boldsymbol{J}(t) = \int \mathrm{d}z\,\boldsymbol{j}(z,t)$ flowing inside the sample [Fig. 1(a)] [38]. Note that a nonzero $\boldsymbol{J}(t)$ requires inversion asymmetry (IA) of the sample. We focus on in-plane magneto-photocurrents due to sample-intrinsic IA (SIA). To minimize contributions by light-induced IA (LIA), in particular, due to pump-intensity gradients inside the sample, films thicker than 50 QL are excluded here but addressed in Supplemental Material Sec. V [29].

To minimize signals from (i) z-directed photocurrents and (ii) in-plane shift currents [39], we (i) choose nearly normal incidence of the pump (Supplemental Material Sec. II [29]) and (ii) set one of the mirror axes of the Bi_2Se_3(111) plane parallel to $\boldsymbol{u}_y$ [Fig. S4(a) [29]].

Raw data—Figure 1(b) shows typical THz waveforms $S_x(t, B_{\rm ext})$ from Bi_2Se_3(16 QL) for opposite magnetic fields $B_{\rm ext} = \pm 0.3$ T. All signals scale linearly with the pump power [Fig. S3(h) [29]]. Remarkably, $S_x(t, B_{\rm ext})$ partially reverses when $B_{\rm ext}$ is reversed. A similar behavior is observed for the other film thicknesses as well (Fig. 5). One can write the THz signal $S_x(t, \pm B_{\rm ext}) = S_{x+}(t) \pm S_{x-}(t)$ as sum of even (S_{x+}) and odd (S_{x-}) components under reversal of $B_{\rm ext}$ with

$$S_{x\pm}(t) = \frac{S_x(t, +B_{\rm ext}) \pm S_x(t, -B_{\rm ext})}{2}, \tag{1}$$

and analogous for $S_{y\pm}$ and $\boldsymbol{J}_{\pm}$.

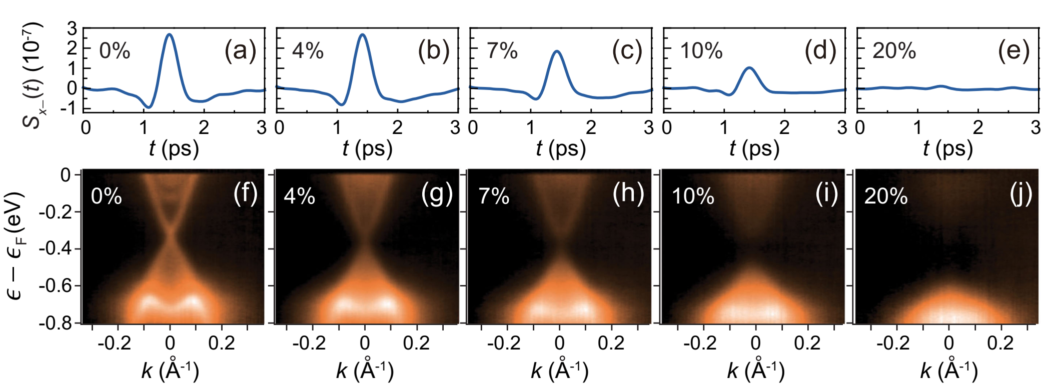

FIG. 2. Impact of indium substitution. (a)–(e) THz magneto-photocurrent signal $S_{x-}(t)$ from $(In_rBi_{1-r})_2Se_3$(30 QL) with an indium content of (a) $r = 0\%$, (b) 4%, (c) 7%, (d) 10%, and (e) 20%, all for $|B_{\rm ext}| = 0.3$ T. (f)–(j) Photoelectron emission intensity vs in-plane electron wave vector k and energy $\epsilon - \epsilon_{\rm F}$ from identical samples for $B_{\rm ext} = 0$ T. The spectra show the disappearance of the TSS at $r > 7\%$ [24]. Panels (f)–(j) are adapted with permission from Ref. [24], Springer Nature.

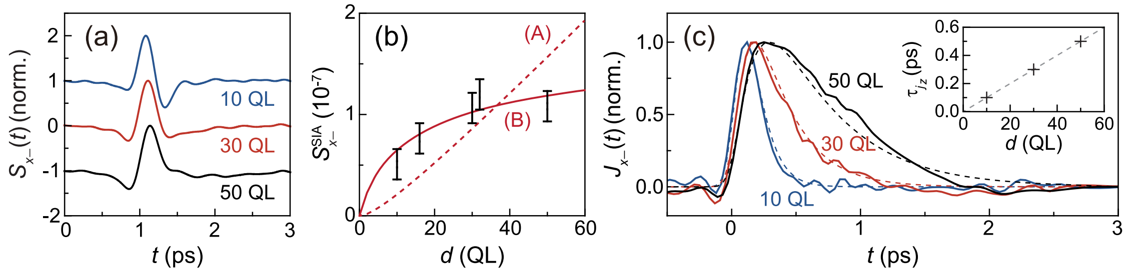

FIG. 3. Bi_2Se_3 thickness variation. (a) THz signals $S_{x-}(t)$ from $Bi_2Se_3(d)$ for $d = 10$, 30, and 50 QL. They are normalized to 1 and displaced by an offset. (b) Amplitude of S_{x-}^{SIA}, i.e., the component of S_{x-} that arises from the SIA of the sample. Fits based on model scenarios (A) and (B) are also shown. (c) Sheet density $J_{x-}(t)$ of the THz magneto-photocurrent extracted from $S_{x-}(t)$. Dashed lines are fits to the data (see main text). The inset shows the extracted relaxation time τ_{j_z} of the photocurrent vs d.

First, S_{x-} reverses nearly completely when the sample is turned by 180° about $\boldsymbol{B}_{\mathrm{ext}} \| \boldsymbol{u}_y$ [Figs. 1(c) and S8 [29]]. It, therefore, predominantly arises from SIA. As S_{x-} is about 50 times larger than S_{y-} [Figs. 1(c) and 6], the associated photocurrent $\boldsymbol{J}_{-}(t)$ is perpendicular to $\boldsymbol{B}_{\mathrm{ext}} = B_{\mathrm{ext}}\boldsymbol{u}_y$. Further, S_{x-} is proportional to B_{ext} [Figs. 1(d), S3(d), S3(f) [29]], but independent of the Bi_2Se_3 azimuth and pump polarization [Figs. S4(c) and S4(d) [29]]. The presence of the selenium cap layer results in only minor changes in S_{x-} (Fig. S6 [29]).

Second, the even-in-B_{ext} part S_{x+} behaves very differently from S_{x-}: It is independent of B_{ext} [Fig. 1(d)] and has a strong pump-polarization dependence [Figs. S4(c) and S4 (d) [29]] and faster dynamics (Fig. S5 [29]). The different behavior suggests that S_{x+} and S_{x-} have very different origins. In fact, S_{x+} is known to predominantly arise from a surface shift current rather than bandlike electron transport [39]. The sizable S_{x+} is not completely quenched in our experiment because the Bi_2Se_3 mirror axis is not perfectly aligned along $\boldsymbol{u}_y$ [Fig. S4(c) [29]]. Consequently, S_x does not fully reverse with B_{ext} [Figs. 1(b), 5, and S9 [29]], and S_{y+} is much larger than S_{y-} (Fig. 6).

Third, any z-directed photocurrent $J_z(t)$ is detected by tilting the sample, such that J_z is partially projected onto the plane of the electro-optic detection [39]. Because J_z changes with B_{ext} only very weakly, it is indistinguishable from the shift current.

All these observations are fully consistent with the C_{3v} point-symmetry group of our sample (Supplemental Material Sec. VI [29]). In the following, we focus on signal S_{x-} [Fig. 1(c)] because it arises from a magnetic-field-dependent photocurrent $J_{x-} \propto B_{\mathrm{ext}}$, i.e., a magneto-photocurrent.

Impact of r and d—To gain more insight into $J_{x-}(t)$, we measure $S_{x-}(t)$ from $(In_rBi_{1-r})_2Se_3$(30 QL) [Figs. 2(a)–2(e)] for $B_{\mathrm{ext}} = \pm 0.3$ T. In these films, the substitution of bismuth by indium modifies the TSS by weakening spin-orbit coupling [25]. Indeed, previous ARPES measurements on samples from the same batch [24] confirm that the TSS band gap opens for $r > 7\%$ [Figs. 2(f)–2(j)].

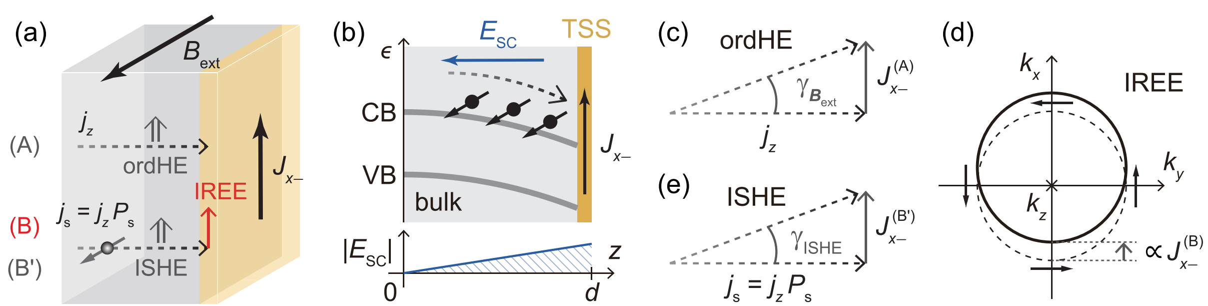

FIG. 4. (a) Schematic of the suggested scenarios (A), (B), and (B') of the magneto-photocurrent. The pump pulse triggers a bulk charge current with density j_z and a spin current $j_s = j_z P_s$ with $P_s \propto B_{\mathrm{ext}}$. Both flow toward the Bi_2Se_3 surface at $z = d$. In scenarios (A) and (B'), respectively, j_z and j_s are converted into an in-plane bulk charge current by the ordHE and ISHE. In scenario (B), the IREE converts j_s into a surface charge current. The resulting sheet density $J_{x-}^{(A)} + J_{x-}^{(B)} + J_{x-}^{(B')}$ emits a THz pulse. (b) Both j_z and j_s arise from the built-in electrostatic field $\boldsymbol{E}_{\mathrm{SC}} = E_{\mathrm{SC}}\boldsymbol{u}_z$ that drives photoexcited electrons toward the TSS at $z = d$ for a duration τ_{j_z}. The indicated qualitative z dependence of the energy ϵ of the bottom of the bulk conduction band (CB) and the top of the valence band (VB) results from $|E_{\mathrm{SC}}| \propto z$. The TSS at $z = 0$ are not shown. (c) The ordHE converts j_z into a transverse current $\gamma_{\boldsymbol{B}_{\mathrm{ext}}} j_z$. (d) In the IREE, injection of j_s into the TSS at $z = d$ shifts the Fermi contour due to spin-velocity locking and, thus, induces a surface charge current. (e) The ISHE converts j_s into a bulk charge current $\gamma_{\mathrm{ISHE}} j_s$.

Figures 2(a)–2(e) reveal that the THz-emission signals $S_{x-}(t)$ have approximately identical shape for all r [Fig. S7(c) [29]]. In contrast, their amplitude exhibits a drastic reduction to 71%, 42%, and 4%, respectively, as r increases from 7% to 10% and 20%. Strikingly, the monotonic amplitude reduction of $S_{x-}(t)$ [Figs. 2(a)–2(e)] is strongly correlated with the decreasing intensity of the TSS in the ARPES spectra [Figs. 2(f)–2(j)]. It is not related to potentially r-dependent pump conditions [Fig. S7(a) [29]].

Finally, we increase the Bi_2Se_3 thickness d from 10 to 50 QL. The shape of the THz signal waveform $S_{x-}(t)$ changes significantly [Fig. 3(a)]. However, the sign of S_{x-} still reverses when the sample is turned by 180° (Fig. S8 [29]). Figure 3(b) displays the signal amplitude that arises from the sample's SIA (Supplemental Material Sec. V [29]). It increases up to $d = 30$ QL, but, importantly, saturates at 50 QL.

It is instructive to extract the dynamics of the charge-current sheet density $J_{x-}(t)$ from $S_{x-}(t)$ [Fig. 3(c)] [38]. Remarkably, as d increases from 10 to 30 and 50 QL, the rise and decay of $J_{x-}(t)$ slow down significantly.

Interpretation—Our THz-emission data imply five essential findings. (F1) S_{x-} and, thus, J_{x-} is independent of the linear pump polarization [Fig. S4(d) [29]]. (F2) S_{x-} changes sign when the sample is turned by 180° [Figs. 1(c) and S8 [29]]. (F3) As the sample thickness increases, the relaxation time of J_{x-} increases [Fig. 3(c)], whereas its amplitude saturates [Fig. 3(b)]. (F4) S_{x-} drops abruptly as the indium fraction in $(In_rBi_{1-r})_2Se_3$ rises [Figs. 2(a)–2(e)] and the TSS intensity in the ARPES spectra is quenched [Figs. 2(f)–2(j)]. (F5) The magneto-photocurrent $\boldsymbol{J}_- = J_{x-}\boldsymbol{u}_x$ is perpendicular and proportional to $\boldsymbol{B}_{\text{ext}} = B_{\text{ext}}\boldsymbol{u}_y$ [Fig. 1(d)].

Finding (F1) implies that shift currents [39] make a minor contribution to J_{x-}. (F2) means that the signal arises predominantly from the sample's SIA for $d \leq 50$ QL. LIA-type contributions due to pump-intensity gradients along the z axis and, thus, Seebeck-type effects are minor [40]. (F3) suggests that J_{x-} involves charge carriers throughout the TI thickness. (F4) indicates that the TSS play an essential role for the generation of J_{x-}.

(F5) can be summarized by the Hall-type relationship $\boldsymbol{J}_- \propto \boldsymbol{u}_z \times \boldsymbol{B}_{\text{ext}}$ [Fig. 1(a)]. To reveal its origin, we note that there are only two fundamental microscopic couplings of a magnetic field $\boldsymbol{B}_{\text{ext}}$ to electrons: (M1) $\boldsymbol{B}_{\text{ext}}$ exerts the Lorentz force $\propto \boldsymbol{v} \times \boldsymbol{B}_{\text{ext}}$ on an electron with velocity $\boldsymbol{v}$. To obtain a current $\propto \boldsymbol{u}_z \times \boldsymbol{B}_{\text{ext}}$, a nonzero mean velocity $\langle \boldsymbol{v} \rangle \| \boldsymbol{u}_z$ is required. (M2) $\boldsymbol{B}_{\text{ext}}$ couples to the electron spin $\boldsymbol{S}$ through Zeeman interaction, which induces an average spin $\langle \boldsymbol{S} \rangle \propto \boldsymbol{B}_{\text{ext}}$ in paramagnetic materials like Bi_2Se_3. Spin-orbit coupling, in turn, exerts a Lorentz-type force $\propto \boldsymbol{v} \times \boldsymbol{S}$ on the electrons in a quasiclassical picture [41]. We obtain a current $\propto \boldsymbol{u}_z \times \boldsymbol{B}_{\text{ext}}$ if $\langle \boldsymbol{v} \rangle \| \boldsymbol{u}_z$.

Note that (M1) and (M2) require, respectively, a charge current j_z and a spin current j_s along $\boldsymbol{u}_z$ [Fig. 4(a)]. We assume that the bulk current j_z of photoexcited electrons is driven by the space-charge field $\boldsymbol{E}_{\text{SC}}$ of the Bi_2Se_3 film [Fig. 4(b)]. It is accompanied by a bulk spin current $j_s = j_z P_s$ because B_{ext} causes a spin polarization $P_s \propto B_{\text{ext}}$. The couplings (M1) vs (M2) naturally lead to three scenarios (A) vs (B), (B') [Fig. 4(a)].

In scenario (A), j_z is converted into a charge current $j_x \propto B_{\text{ext}}$ in the bulk by the Lorentz force of (M1) and, thus, the ordinary Hall effect (ordHE) [Figs. 4(a) and 4(c)]. In scenarios (B) and (B'), $j_s = j_z P_s \propto j_z B_{\text{ext}}$ is converted into a charge current j_x by the spin-orbit coupling of (M2) [Fig. 4(a)]. Such SCC has two flavors: the inverse Rashba Edelstein effect (IREE) at the Bi_2Se_3 surface and the inverse spin Hall effect (ISHE) in the bulk [20]. Accordingly, in scenario (B), j_s is injected into the TSS at $z = d$, where the IREE leads to a surface charge current [Figs. 4(a) and 4(d)]. In (B'), j_s is converted into a charge current throughout the TI bulk by the ISHE [Figs. 4(a) and 4(e)].

While all three scenarios are consistent with the symmetry properties of signal $S_{x-}(t)$, scenario (B) explains our findings quantitatively significantly better. We, thus, consider it first.

Scenario (B)—The big picture and its steps (B1)–(B3) are summarized in Figs. 4(a), 4(b), and 4(d). (B1) The external magnetic field $\boldsymbol{B}_{\text{ext}}$ causes a spin polarization $P_s \propto B_{\text{ext}}$ of the Bi_2Se_3 bulk electrons. We estimate $P_s = 0.3\%$ for $B_{\text{ext}} = 0.3$ T.

(B2) Photoexcitation together with the built-in space-charge field $\boldsymbol{E}_{\text{SC}} = E_{\text{SC}}\boldsymbol{u}_z$ of the Bi_2Se_3 film [Fig. 4(b)] launches an electron current $j_z \propto E_{\text{SC}}$ with spin polarization P_s toward the Bi_2Se_3 surface. Its relaxation time τ_{j_z} equals the mean time for the photoexcited bulk electrons to drift toward the surface.

(B3) The associated spin-current density $j_s = j_z P_s$ induces a spin-polarized occupation of the TSS. Owing to spin-velocity locking, a charge current with sheet density $J_{x-}^{(\text{B})}$ perpendicular to B_{ext} results [Fig. 4(d)]. Indeed, TSS are known to have a large IREE and, thus, SCC efficiency [42]. In Appendix C and Supplemental Material Sec. VII [29], we discuss the plausibility of model steps (B1)–(B3) and derive the resulting dynamics of the magneto-photocurrent $J_{x-}^{(\text{B})}$ [Eq. (C2)].

As seen in Fig. 3(c), we obtain excellent fits of $J_{x-}^{(\text{B})}$ to our measured J_{x-} waveforms, where the momentum relaxation time τ_{TSS} of the TSS, the j_z relaxation time τ_{j_z} and an overall amplitude scaling are fit parameters. The extracted $\tau_{\text{TSS}} \approx 100$ fs determines the rise time of $J_{x-}^{(\text{B})}$ [Fig. 3(c)] and agrees with previously inferred values [26,28]. The modeled ($8\ \text{A m}^{-1}$) and measured peak magnitude ($5\ \text{A m}^{-1}$) of the current sheet density J_{x-} agree well, too.

The observed linear increase of the relaxation time τ_{j_z} with the TI thickness d [inset of Fig. 3(c)] is in line with $\tau_{j_z} \propto 1/n_0$ [Eq. (C1)] and the space-charge density $n_0 = N_{\text{SC}}/d$ that arises from the selenium vacancies (Fig. S11 [29]) with sheet density $N_{\text{SC}} \sim 10^{12}\ \text{cm}^{-2}$ [43].

The relaxation time τ_{j_z} of J_{x-} in $(\mathrm{In}_r\mathrm{Bi}_{1-r})_2\mathrm{Se}_3(30\ \mathrm{QL})$ depends on r only weakly [Fig. S7(e) [29]], suggesting that the space-charge field remains persistent vs r. As $\tau_{j_z} \leq 0.5$ ps is substantially faster than the typical electron-hole recombination time (≈2 ps) of Bi_2Se_3 [44], the latter is not visible in our current traces [Fig. 3(c)]. Interestingly, in the ultrafast ARPES signal from TSS [44], the extended rise time of ≈0.5 ps could be interpreted as fingerprint of τ_{j_z} and, thus, the photocurrent j_z.

To summarize, we find good agreement between the observed and modeled dynamics, time constants and magnitude of the magneto-photocurrent sheet density J_{x-}. This agreement indicates that scenario (B) captures the crucial features of the underlying mechanisms.

Comparison to (B') and (A)—In scenario (B'), the spin current $j_s = j_z P_s$ is converted into a charge current with density $j_{x-}^{(B')} = \gamma_{\mathrm{ISHE}} j_s$ by the ISHE [Fig. 4(e)] throughout the bulk [Fig. 4(a)]. By z integration of $j_{x-}^{(B')}$ and with $\gamma_{\mathrm{ISHE}} \sim 0.1$ for the ISHE angle of Bi_2Se_3 [8], we obtain a sheet density $J_{x-}^{(B')} \sim 0.1\ \mathrm{A\ m^{-1}}$, which is 1 order of magnitude smaller than the measured value. Therefore, scenario (B') can be disregarded.

In scenario (A), the charge current j_z is converted into an in-plane charge current by the ordHE [Fig. 4(c)]. According to Eq. (D1), $J_{x-}^{(A)}$ rises and decays with the time constants of, respectively, τ_{bulk} and τ_{j_z}, where τ_{bulk} is the bulk momentum relaxation time. This shape agrees with the experiment [Fig. 3(c)], and the estimated peak $J_{x-}^{(A)} \sim 3\ \mathrm{A\ m^{-1}}$ is comparable with the measured $5\ \mathrm{A\,m^{-1}}$.

The agreement of scenario (A) and our experimental data should be taken with caution. First, the modeled $J_{x-}^{(A)}$ is overestimated because our model ignores that electrons and holes contribute to $J_{x-}^{(A)}$ with opposite sign [45]. Second, the $\tau_{\mathrm{bulk}} = 37$ fs of the Bi_2Se_3 bulk (Table S1 [29]) is significantly smaller than the observed rise time of J_{x-} of ≈100 fs for $r \leq 10\%$ [Figs. S7(d) and S7(e) [29]].

Third, and most importantly, the in-plane charge currents in scenario (B) and (A) flow, respectively, at the Bi_2Se_3 surface [Eq. (C2)] and throughout the Bi_2Se_3 bulk [Eq. (D1)]. Therefore, the current sheet density J_{x-} scales differently with the sample thickness. Scenario (B) explains the saturation of the photocurrent for $d > 30$ QL well [Fig. 3(b)], whereas (A) implies a quasilinear increase with d (Supplemental Material Sec. V [29]). These three arguments indicate that scenario (A) makes a minor contribution to the observed magneto-photocurrent.

Scenario (B) can further rationalize the impact of indium substitution (Fig. 2): As r increases, the TSS intensity in the ARPES spectra decreases [Figs. 2(f)–2(j)], and so does the strength of the IREE [Fig. 4(d)] and the THz signal S_{x-} [Figs. 2(a)–2(e)]. Interestingly, at $r = 10\%$, the Dirac point is not visible anymore [Fig. 2(i)], whereas S_{x-} is still substantial [Fig. 2(d)]. This observation suggests the presence of an IREE without TSS [46], which vanishes at $r = 20\%$ [Fig. 2(e)]. To summarize, scenario (B) is consistent with all findings (F1)–(F5) of our experiment.

Conclusion—We observe THz photocurrents in the three-dimensional topological insulator Bi_2Se_3 as a function of an in-plane magnetic field $\boldsymbol{B}_{\mathrm{ext}}$. It has two components. The first is independent of $\boldsymbol{B}_{\mathrm{ext}}$ and arises from surface-localized shift currents [39]. The second component is perpendicular and proportional to $\boldsymbol{B}_{\mathrm{ext}}$. It can consistently be explained by a spin-polarized out-of-plane current of optically excited electrons in the TI bulk that is converted into an in-plane charge current by the IREE at the TI surface [Figs. 4(a), 4(b), and 4(d)].

Interestingly, at a magnetic field of 0.3 T, the magneto-photocurrent is only 1 order of magnitude smaller than in stacks of ferromagnetic Co and the TI Bi_2Te_3 [42]. We believe that this relatively strong amplitude is a result of very efficient spin injection from the Bi_2Se_3 bulk into TSS.

Importantly, THz magneto-photocurrents allow us to characterize the SCC efficiency of TSS without the need to attach ferromagnetic thin films that may strongly perturb the TI. We expect that our method can be transferred to other three-dimensional TIs and, more generally, paramagnetic materials to study their SCC capabilities. If the sample lacks SIA, one can simply employ LIA.

Acknowledgments—C. I. acknowledges support by the National Research Foundation of Korea (Grant No. 2021R1A6A3A14044225). D. J. and S. O. thank the Army Research Office's No. W911NF2010108 and No. MURI W911NF2020166. G. B., T. S. S., and T. K. acknowledge funding by the European Research Council through ERC-2023 AdG ORBITERA (Grant No. 101142285), the European Union H2020 program through the FET project SKYTOP (Grant No. 824123) and by the Deutsche Forschungsgemeinschaft (DFG, German Research Foundation) through project ACEs (Project No. 544376304), the Collaborative Research Center SFB TRR 227 "Ultrafast spin dynamics" (Project No. 328545488; Projects A05 and B02) and the Excellence Cluster EXC 3112 "Center for Chiral Electronics" (EXC 3112/1, Project No. 533767171).

Data availability—The data that support the findings in the article are openly available [47]. The data for Supplemental Material [29] are available upon reasonable request from the authors.

[1] Q. L. He, T. L. Hughes, N. P. Armitage, Y. Tokura, and K. L. Wang, Topological spintronics and magnetoelectronics, Nat. Mater. **21**, 15 (2022).

[2] H. Wang *et al.*, Room temperature energy-efficient spin-orbit torque switching in two-dimensional van der Waals Fe_3GeTe_2 induced by topological insulators, Nat. Commun. **14**, 5173 (2023).

[3] D. Chaudhuri, M. Salehi, S. Dasgupta, M. Mondal, J. Moon, D. Jain, S. Oh, and N. P. Armitage, Ambipolar magneto-optical response of ultralow carrier density topological insulators, Phys. Rev. B **103**, L081110 (2021).

[4] R. Fujimura, R. Yoshimi, M. Mogi, A. Tsukazaki, M. Kawamura, K. S. Takahashi, M. Kawasaki, and Y. Tokura, Current-induced magnetization switching at charge-transferred interface between topological insulator $(Bi, Sb)_2Te_3$ and van der Waals ferromagnet Fe_3GeTe_2, Appl. Phys. Lett. **119**, 032402 (2021).

[5] P. He, S. S. L. Zhang, D. Zhu, S. Shi, O. G. Heinonen, G. Vignale, and H. Yang, Nonlinear planar Hall effect, Phys. Rev. Lett. **123**, 016801 (2019).

[6] H. Soifer *et al.*, Band-resolved imaging of photocurrent in a topological insulator, Phys. Rev. Lett. **122**, 167401 (2019).

[7] K. N. Okada, N. Ogawa, R. Yoshimi, A. Tsukazaki, K. S. Takahashi, M. Kawasaki, and Y. Tokura, Enhanced photogalvanic current in topological insulators via Fermi energy tuning, Phys. Rev. B **93**, 081403(R) (2016).

[8] M. Jamali, J. S. Lee, J. S. Jeong, F. Mahfouzi, Y. Lv, Z. Zhao, B. K. Nikolić, K. A. Mkhoyan, N. Samarth, and J. P. Wang, Giant spin pumping and inverse spin Hall effect in the presence of surface and bulk spin-orbit coupling of topological insulator Bi_2Se_3, Nano Lett. **15**, 7126 (2015).

[9] S. Zhang and A. Fert, Conversion between spin and charge currents with topological insulators, Phys. Rev. B **94**, 184423 (2016).

[10] E. Longo, L. Locatelli, P. Tsipas, A. Lintzeris, A. Dimoulas, M. Fanciulli, M. Longo, and R. Mantovan, Exploiting the close-to-dirac point shift of the Fermi level in the Sb_2Te_3/Bi_2Te_3 topological insulator heterostructure for spin-charge conversion, ACS Appl. Mater. Interfaces **15**, 50237 (2023).

[11] E. Longo *et al.*, Large spin-to-charge conversion at room temperature in extended epitaxial Sb_2Te_3 topological insulator chemically grown on silicon, Adv. Funct. Mater. **32**, 2109361 (2022).

[12] H. Wu *et al.*, Room-temperature spin-orbit torque from topological surface states, Phys. Rev. Lett. **123**, 207205 (2019).

[13] H. Wang, J. Kally, J. S. Lee, T. Liu, H. Chang, D. R. Hickey, K. A. Mkhoyan, M. Wu, A. Richardella, and N. Samarth, Surface-state-dominated spin-charge current conversion in topological-insulator-ferromagnetic-insulator heterostructures, Phys. Rev. Lett. **117**, 076601 (2016).

[14] A. R. Mellnik *et al.*, Spin-transfer torque generated by a topological insulator, Nature (London) **511**, 449 (2014).

[15] Y. Wang *et al.*, Room temperature magnetization switching in topological insulator-ferromagnet heterostructures by spin-orbit torques, Nat. Commun. **8**, 1364 (2017).

[16] X. Wang *et al.*, Ultrafast spin-to-charge conversion at the surface of topological insulator thin films, Adv. Mater. **30**, 1802356 (2018).

[17] E. Rongione *et al.*, Ultrafast spin-charge conversion at $SnBi_2Te_4/Co$ topological insulator interfaces probed by terahertz emission spectroscopy, Adv. Opt. Mater. **10**, 2102061 (2022).

[18] H. Park *et al.*, Enhanced spin-to-charge conversion efficiency in ultrathin Bi_2Se_3 observed by spintronic terahertz spectroscopy, ACS Appl. Mater. Interfaces **13**, 23153 (2021).

[19] X. Chen *et al.*, Generation, and control of terahertz spin currents in topology-induced 2D ferromagnetic $Fe_3GeTe_2|Bi_2Te_3$ heterostructures, Adv. Mater. **34**, 2106172 (2022).

[20] A. Manchon, J. Železný, I. M. Miron, T. Jungwirth, J. Sinova, A. Thiaville, K. Garello, and P. Gambardella, Current-induced spin-orbit torques in ferromagnetic and antiferromagnetic systems, Rev. Mod. Phys. **91**, 035004 (2019).

[21] J. Zhang, J. P. Velev, X. Dang, and E. Y. Tsymbal, Band structure and spin texture of Bi_2Se_3 3d ferromagnetic metal interface, Phys. Rev. B **94**, 014435 (2016).

[22] A. Wolos *et al.*, G-factors of conduction electrons and holes in Bi_2Se_3 three-dimensional topological insulator, Phys. Rev. B **93**, 155114 (2016).

[23] O. Ly and D. M. Basko, Theory of electron spin resonance in bulk topological insulators Bi_2Se_3, Bi_2Te_3 and Sb_2Te_3, J. Phys. Condens. Matter **28**, 155801 (2016).

[24] C. Heide *et al.*, Probing topological phase transitions using high-harmonic generation, Nat. Photonics **16**, 620 (2022).

[25] M. Brahlek, N. Bansal, N. Koirala, S. Y. Xu, M. Neupane, C. Liu, M. Z. Hasan, and S. Oh, Topological-metal to band-insulator transition in $(Bi_{1-x}In_x)_2Se_3$ thin films, Phys. Rev. Lett. **109**, 186403 (2012).

[26] L. Wu, M. Brahlek, R. Valdés Aguilar, A. V Stier, C. M. Morris, Y. Lubashevsky, L. S. Bilbro, N. Bansal, S. Oh, and N. P. Armitage, A sudden collapse in the transport lifetime across the topological phase transition in $(Bi_{1-x}In_x)_2Se_3$, Nat. Phys. **9**, 410 (2013).

[27] N. Bansal, Y. S. Kim, M. Brahlek, E. Edrey, and S. Oh, Thickness-independent transport channels in topological insulator Bi_2Se_3 thin films, Phys. Rev. Lett. **109**, 116804 (2012).

[28] R. V. Aguilar *et al.*, Terahertz response and colossal kerr rotation from the surface states of the topological insulator Bi_2Se_3, Phys. Rev. Lett. **108**, 087403 (2012).

[29] See Supplemental Material at http://link.aps.org/supplemental/10.1103/yvbq-rdkz for sample characterization, current-to-field conversion, more THz-emission data, impact of indium content, TI thickness, and signal phenomenology and model details, which includes Refs. [30–37].

[30] T. Yoshino, Theory for oblique-incidence magneto-optical Faraday and Kerr effects in interfaced monolayer graphene and their characteristic features, J. Opt. Soc. Am. B **30**, 1085 (2013).

[31] L. Wu, W. K. Tse, M. Brahlek, C. M. Morris, R. V. Aguilar, N. Koirala, S. Oh, and N. P. Armitage, High-resolution Faraday rotation and electron-phonon coupling in surface states of the bulk-insulating topological insulator $Cu_{0.02}Bi_2Se_3$, Phys. Rev. Lett. **115**, 217602 (2015).

[32] J. G. Analytis, J. H. Chu, Y. Chen, F. Corredor, R. D. McDonald, Z. X. Shen, and I. R. Fisher, Bulk Fermi surface coexistence with Dirac surface state in Bi_2Se_3: A comparison of photoemission and Shubnikov–de Haas measurements, Phys. Rev. B **81**, 205407 (2010).

[33] J. W. McIver, D. Hsieh, S. G. Drapcho, D. H. Torchinsky, D. R. Gardner, Y. S. Lee, and N. Gedik, Theoretical and experimental study of second harmonic generation from the

surface of the topological insulator Bi_2Se_3, Phys. Rev. B **86**, 035327 (2012).

[34] R. Rouzegar *et al.*, Laser-induced terahertz spin transport in magnetic nanostructures arises from the same force as ultrafast demagnetization, Phys. Rev. B **106**, 144427 (2022).

[35] J. A. Sobota, S. Yang, J. G. Analytis, Y. L. Chen, I. R. Fisher, P. S. Kirchmann, and Z. X. Shen, Ultrafast optical excitation of a persistent surface-state population in the topological insulator Bi_2Se_3, Phys. Rev. Lett. **108**, 117403 (2012).

[36] J. Humlíček, D. Hemzal, A. Dubroka, O. Caha, H. Steiner, G. Bauer, and G. Springholz, Raman and interband optical spectra of epitaxial layers of the topological insulators Bi_2Te_3 and Bi_2Se_3 on BaF_2 substrates, Phys. Scr. Top. Issues **T162**, 014007 (2014).

[37] Z. Zhang and J. T. Yates, Band bending in semiconductors: Chemical and physical consequences at surfaces and interfaces, Chem. Rev. **112**, 5520 (2012).

[38] T. S. Seifert *et al.*, Femtosecond formation dynamics of the spin seebeck effect revealed by terahertz spectroscopy, Nat. Commun. **9**, 2899 (2018).

[39] L. Braun, G. Mussler, A. Hruban, M. Konczykowski, T. Schumann, M. Wolf, M. Münzenberg, L. Perfetti, and T. Kampfrath, Ultrafast photocurrents at the surface of the three-dimensional topological insulator Bi_2Se_3, Nat. Commun. **7**, 13259 (2016).

[40] K. Takahashi, T. Kanno, A. Sakai, H. Tamaki, H. Kusada, and Y. Yamada, Terahertz radiation via ultrafast manipulation of thermoelectric conversion in thermoelectric thin films, Adv. Opt. Mater. **2**, 428 (2014).

[41] E. M. Chudnovsky, Theory of spin Hall effect: Extension of the drude model, Phys. Rev. Lett. **99**, 206601 (2007).

[42] G. Bierhance *et al.*, Terahertz time-domain signatures of the inverse edelstein effect in topological-insulator/ferromagnet heterostructures, Phys. Rev. Appl. **25**, 024054 (2026).

[43] N. Koirala *et al.*, Record surface state mobility and quantum Hall effect in topological insulator thin films via interface engineering, Nano Lett. **15**, 8245 (2015).

[44] Y. H. Wang, D. Hsieh, E. J. Sie, H. Steinberg, D. R. Gardner, Y. S. Lee, P. Jarillo-Herrero, and N. Gedik, Measurement of intrinsic Dirac fermion cooling on the surface of the topological insulator Bi_2Se_3 using time-resolved and angle-resolved photoemission spectroscopy, Phys. Rev. Lett. **109**, 127401 (2012).

[45] L. G. Zhu, B. Kubera, K. Fai Mak, and J. Shan, Effect of surface states on terahertz emission from the Bi_2Se_3 surface, Sci. Rep. **5**, 10308 (2015).

[46] G. Bihlmayer, P. Noël, D. V. Vyalikh, E. V. Chulkov, and A. Manchon, Rashba-like physics in condensed matter, Nat. Rev. Phys. **4**, 642 (2022).

[47] C. In, G. Bierhance, D. Jain, T. S. Seifert, O. Gueckstock, R. Mantovan, S. Oh, and T. Kampfrath, Data for In *et al.* "Terahertz magneto-photocurrents in the topological insulator Bi_2Se_3 probe its topological surface states," Zenodo, 10.5281/zenodo.21610511 (2026).

[48] D. Hsieh *et al.*, Observation of time-reversal-protected single-Dirac-cone topological-insulator states in Bi_2Te_3 and Sb_2Te_3, Phys. Rev. Lett. **103**, 146401 (2009).

[49] D. Hsieh *et al.*, A tunable topological insulator in the spin helical dirac transport regime, Nature (London) **460**, 1101 (2009).

[50] D. Hsieh, J. W. McIver, D. H. Torchinsky, D. R. Gardner, Y. S. Lee, and N. Gedik, Nonlinear optical probe of tunable surface electrons on a topological insulator, Phys. Rev. Lett. **106**, 057401 (2011).

[51] J. Reimann *et al.*, Subcycle observation of lightwave-driven dirac currents in a topological surface band, Nature (London) **562**, 396 (2018).

[52] J. Shan, T. F. Heinz, C. Weiss, R. Wallenstein, and R. Beigang, Origin of magnetic field enhancement in the generation of THz radiation from semiconductor surfaces, Opt. Lett. **26**, 849 (2001).

End Matter

Appendix A: THz signals S_x for various d—Figures 5(a)–5(c) show THz signals $S_x(t, \pm B_{\rm ext})$ at $\boldsymbol{B}_{\rm ext} = B_{\rm ext}\boldsymbol{u}_y$ with $|B_{\rm ext}| = 0.3$ T for three Bi_2Se_3 thicknesses up to 50 QL. Each signal $S_x(t, \pm B_{\rm ext}) = S_{x+}(t) \pm S_{x-}(t)$ is a linear superposition of signals S_{x-} and S_{x+} odd and even in $B_{\rm ext}$ [Eq. (1)]. Both components have comparable order of magnitude.

A variation of $B_{\rm ext}$ shows that S_{x-} is linear in $B_{\rm ext}$ and S_{x+} is independent of $B_{\rm ext}$ [Fig. 1(d)]. Therefore, S_{x-} and S_{x+} add up independently of each other (see Supplemental

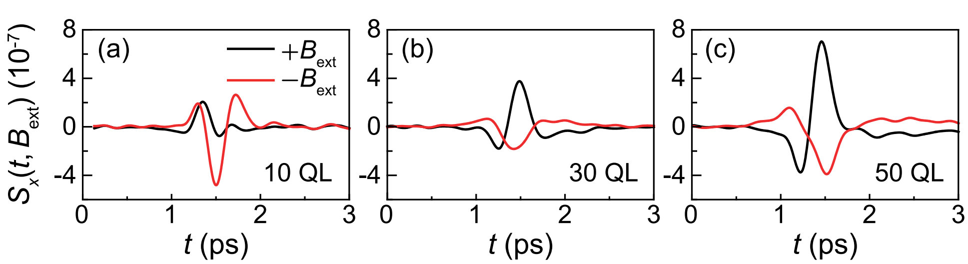

FIG. 5. THz signals $S_x(t, \pm B_{\rm ext})$ for $|B_{\rm ext}| = 0.3$ T from Bi_2Se_3 with thicknesses of (a) $d = 10$ QL, (b) 30 QL, and (c) 50 QL.

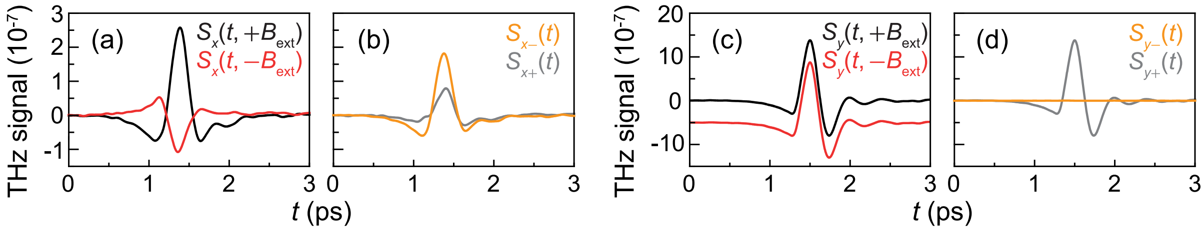

FIG. 6. THz signals from Bi_2Se_3(16 QL) with $B_{ext} = 0.3$ T. (a) Signals $S_x(t, +B_{ext})$ and $S_x(t, -B_{ext})$ and (b) the resulting components $S_{x+}(t)$ and $S_{x-}(t)$. Similarly, (c) $S_y(t, \pm B_{ext})$ and (d) $S_{y\pm}(t)$. In panel (c), $S_y(t, -B_{ext})$ is vertically offset.

Material Sec. V [29]). Similarly, all mechanisms contributing to S_{x-} add up independently as their currents are linear in B_{ext}.

Appendix B: Additional odd and even signal components—Figure 6(a) shows the raw signals $S_x(t, \pm B_{ext})$ identical to Fig. 1(b). Following Eq. (1), THz signals $S_{x\pm}(t)$ even and odd in the external magnetic field $\boldsymbol{B}_{ext} = B_{ext}\boldsymbol{u}_y$ with $B_{ext} = 0.3$ T are displayed in Fig. 6(b). The raw signals $S_y(t, \pm B_{ext})$ and resulting components $S_{y\pm}(t)$ are shown in Figs. 6(c) and 6(d). Because $S_y(t, +B_{ext})$ and $S_y(t, -B_{ext})$ are approximately identical, the odd-in-B_{ext} THz component $S_{y-}(t)$ [Fig. 6(d)] is more than 2 orders of magnitude smaller than the even-in-B_{ext} part $S_{y+}(t)$. The S_{y+} amplitude is proportional to $\cos(3\varphi_A + 2\varphi_P)$, analogous to $S_{x+} \propto \sin(3\varphi_A + 2\varphi_P)$ in Figs. S4(c) and S4(d) [29]. The amplitude of S_{y-} is about 2% of S_{x-}.

Appendix C: Steps of scenario (B)—We discuss the plausibility of steps (B1)–(B3) of scenario (B) [Fig. 4(a)] in the framework of a simple analytical model. More details can be found in Supplemental Material Sec. VII [29].

(B1) We assume Pauli paramagnetism where the external magnetic field shifts spin-up and spin-down bands of the Bi_2Se_3 bulk electrons by an energy $\pm g_s\mu_B B_{ext}$. Here, $g_s \approx 2$ is the g factor of the free electron, and μ_B is the Bohr magneton. The induced spin density $N_\uparrow - N_\downarrow = g_s\mu_B B_{ext} D_e(\epsilon_F)$ scales with the electronic density of states D_e at the Fermi energy ϵ_F. In our sample, the known band structure [48,49] and known $\epsilon_F \sim 15$ meV [27] imply a spin polarization of $P_s = (N_\uparrow - N_\downarrow)/(N_\uparrow + N_\downarrow) \approx 0.3\%$ for $B_{ext} = 0.3$ T. The initial pump-induced photoexcited spin density of $\Delta(N_\uparrow - N_\downarrow)_0 \sim 10^{22}\ \mathrm{m^{-3}}$ is estimated by multiplying the excited electron density $\Delta(N_\uparrow + N_\downarrow)_0$ with P_s.

(B2) Bi_2Se_3 has an internal space-charge field $\boldsymbol{E}_{SC} = E_{SC}\boldsymbol{u}_z$ along the z axis. It arises from positively charged selenium vacancies at the Bi_2Se_3 interface and is modeled by $E_{SC}(z) = -Z_0 c e n_0 z/\varepsilon_{DC}$ [see Figs. 4(b) and S11 [29]] [27,33,50]. Here, n_0 is the homogeneous spatial charge density, Z_0 is the vacuum impedance, c is the light velocity in vacuum, and ε_{DC} is the static dielectric function. E_{SC} accelerates the photoexcited electrons to a local drift velocity $v_e(z) = -\mu_e E_{SC}(z) = z/\tau_{j_z}$, where $\mu_e > 0$ is the bulk electron mobility and

$$\tau_{j_z} := \frac{\varepsilon_{DC}}{Z_0 c e n_0 \mu_e}. \tag{C1}$$

The resulting current density $j_z(z,t) = \Delta(N_\uparrow + N_\downarrow)(t) v_e(z)$ and its dynamics are determined by charge conservation and possible relaxation of the photoexcited carriers. At the TI-air interface ($z = d$), we obtain $j_z(d,t) = A_{j_z}\Theta(t)e^{-t/\tau_{j_z}}$ with $A_{j_z} = \Delta(N_\uparrow + N_\downarrow)_0 d/\tau_{j_z}$ and the Heaviside step function $\Theta(t)$. Therefore, τ_{j_z} [Eq. (C1)] sets the relaxation time of the charge current j_z and spin current $j_s = j_z P_s$. It equals the mean time for the photoexcited bulk electrons to drift toward the surface (Supplemental Material Sec. VII [29]).

(B3) The j_s arriving at the surface $z = d$ leads to spin accumulation in the TSS, which, due to spin-velocity locking, results in an in-plane charge current with sheet density J_{x-} proportional to the accumulated spin sheet density (IREE) [Fig. 4(d)]. Assuming the surface current flows at the TSS group velocity v_{TSS} and decays with the time constant τ_{TSS}, we find that

$$J_{x-}^{(B)}(t) = [H_{TSS} * (j_z P_s)](t)|_{z=d}. \tag{C2}$$

Thus, $J_{x-}^{(B)}(t)$ equals the convolution ($*$) of the spin current $j_s = j_z P_s$ at $z = d$ and the TSS relaxation function $H_{TSS}(t) = v_{TSS}\Theta(t)e^{-t/\tau_{TSS}}$ [51]. From right to left, the three terms of Eq. (C2) summarize the three steps discussed above: (B1) spin polarization $P_s \propto B_{ext}$, (B2) drift of the photoexcited electrons in the space-charge field [j_z, Fig. 4(b)], and (B3) SCC in TSS [H_{TSS}, Fig. 4(d)]. According to Eq. (C2) and for $\tau_{TSS} \ll \tau_{j_z}$, $J_{x-}^{(B)}$ rises and decays exponentially with the time constants τ_{TSS} and τ_{j_z}, respectively.

The modeled ($v_{TSS}\tau_{TSS}A_{j_z}P_s \approx 8\ \mathrm{A\ m^{-1}}$) and measured peak magnitude ($\approx 5\ \mathrm{A\ m^{-1}}$) of the current sheet density J_{x-} agree well. Our model further implies $\tau_{j_z} \propto 1/n_0$ [Eq. (C1)] with the space-charge density $n_0 = N_{SC}/d$ of the electrons and the sheet density N_{SC} of the selenium vacancies (Fig. S11 [29]). Thus, the mean duration τ_{j_z} of electrons to traverse the Bi_2Se_3 film increases linearly with the film thickness d.

Appendix D: Scenario (A)—Here, the charge photocurrent j_z is converted into a transverse charge current by the ordHE [Fig. 4(c)]. The conversion is characterized by the Hall angle $\gamma_{\boldsymbol{B}_\mathrm{ext}} \sim \mu_\mathrm{e} B_\mathrm{ext}$, the electron mobility μ_e and the momentum relaxation time τ_bulk of the bulk electrons [52]. The resulting magneto-photocurrent sheet density is given by the convolution

$$J_{x-}^{(\mathrm{A})}(t) = \left(H_\mathrm{ordHE} * \int \mathrm{d}z\, j_z\right)(t) \tag{D1}$$

with $H_\mathrm{ordHE}(t) = (\gamma_{\boldsymbol{B}_\mathrm{ext}}/\tau_\mathrm{bulk})\Theta(t)\mathrm{e}^{-t/\tau_\mathrm{bulk}}$ (Supplemental Material Sec. VII [29]). The z integration arises because the ordHE proceeds through the whole Bi_2Se_3 thickness [Fig. 4(a)].